Design of a new turbulent dynamo experiment on the OMEGA-EP

Andy Sha Liao, Shengtai Li, Hui Li, Kirk Flippo (iD), Daniel Barnak, Kwyntero Van Kelso, Codie Fiedler Kawaguchi, Alexander Rasmus, Sallee Klein, Joseph Levesque (iD), Carolyn Kuranz, and Chikang Li

View Online

Export Citation

CrossMark

ARTICLES YOU MAY BE INTERESTED IN

Design of a new turbulent dynamo experiment on the OMEGA-EP

View Online   Export Citation   CrossMark

Andy Sha Liao,[1,a)] Shengtai Li,[1] Hui Li,[1] Kirk Flippo,[2] (iD) Daniel Barnak,[2] Kwyntero Van Kelso,[2]
Codie Fiedler Kawaguchi,[2] Alexander Rasmus,[2,3] Sallee Klein,[3] Joseph Levesque,[3] (iD) Carolyn Kuranz,[3]
and Chikang Li[4]

AFFILIATIONS

[1]Theoretical Division, Los Alamos National Laboratory, Los Alamos, New Mexico 87545, USA
[2]Physics Division, Los Alamos National Laboratory, Los Alamos, New Mexico 87545, USA
[3]Climate and Space Sciences and Engineering Department, University of Michigan, Ann Arbor, Michigan 48109, USA
[4]Plasma Science and Fusion Center, Massachusetts Institute of Technology, Cambridge, Massachusetts 02139, USA

a)Author to whom correspondence should be addressed: aliao@lanl.gov

ABSTRACT

Turbulent dynamos that exponentially amplify initially small, seed magnetic fields are crucial in magnetizing the Galaxy and beyond. Until now, the ideal environment for turbulent dynamos to grow has been difficult to recreate. In a new approach, we leverage the long pulse capability of the OMEGA-EP laser to recreate the highly conductive and inviscid ($Re_m \sim 5500$, $Pr_m \gtrsim 1$) growth environment of the turbulent dynamo within the magnetized plasma jet ablated from a simple cone target of CH plastic. In 3-D FLASH simulations of our scheme, we find that the ideal dynamo environment is a typically $\sim 1\,mm^3$, $\gtrsim 1.5\,keV$ hot spot where the laser beams intersect to produce maximum direct heating of the jet plasma. The dynamo environment is maintained from the onset of steady flows through the $\sim 10\,ns$ length of the laser pulse. For a plasma vorticity of 0.3–$3.0\,ns^{-1}$ and a dynamo active over $\sim 5\,ns$, the magnetic energy increases on an exponential trajectory by more than a decade. Fourier analysis reveals that the dynamo progressively saturates up to $E_B/E_K \sim 20\%$ from small scales $k \gtrsim 30\,cm^{-1}$ to large in the time it is sustained. We find robust agreement between the evolution of magnetic energy spectra extracted from the FLASH physics simulation and that derived from synthetic sheath-accelerated proton deflectometry images, thereby demonstrating that the dynamo activity can be quantified in a real experiment.

I. INTRODUCTION

The turbulent dynamo (TMD), powered by the incoherent motion of turbulent plasma,[1–3] is a keystone of the Galactic ecosystem. It exponentially amplifies weak seed magnetic fields arising from intrinsic battery processes, e.g., in supernovae, into the much stronger magnetic fields that are actually observed in the interstellar medium (ISM).[4,5]

Supernovae also seed the ISM with the turbulence energy that drives the TMD.[6,7] In turn, the interstellar turbulence and TMD-amplified magnetic fields profoundly affect the stellar population synthesis, whose influence on the future production of supernovae acts on the interstellar TMD as a feedback control.[8,9] Hence, properly understanding the TMD mechanics, in the ISM and elsewhere it is active, is crucial to accurately predicting the structural, chemical, and energetic evolution of the Galaxy.

In recent years, computational techniques have advanced to allow large-scale, high resolution, magnetohydrodynamical (MHD) models of supernovae-driven interstellar turbulence to proliferate.[10–12] These computational models have enabled key discoveries on the relationships between the trajectory and saturation of the TMD and the distribution and dissipation of turbulence and magnetic energy, thereby improving our understanding of the TMD in a wide range of idealized scenarios.[13–16]

In contrast, laboratory models of the TMD have been limited in scope due to the difficulty of experimentally recreating the astrophysical conditions where the TMD can exist. Nevertheless, traditional liquid sodium platforms have demonstrated, albeit inconclusively, the TMD activity in the resistive dissipation-dominated regimes that are analogous to solar or planetary environments.[17,18] Recent experiments using high power lasers have further extended the reach of the

laboratory TMD to the high energy density (HED) regime.[19,20] Despite these advances in experimental techniques, no laboratory experiment has attempted to reproduce the TMD in the viscous dissipation-dominated regime that describes the ISM.

In this article, we introduce a new experimental platform to recreate the viscous dissipation-dominated TMD (VTMD) using the OMEGA-EP laser in Sec. II. We show in Sec. III that the results of numerical simulations of our experimental platform not only validate our scheme but also suggest further-reaching impacts that we will discuss in Sec. IV. We summarize our findings in Sec. V with a view towards further optimizing and generalizing our OMEGA-EP experimental platform.

II. EXPERIMENTAL PLATFORM

A. Creating the turbulent dynamo

We design the experimental platform shown in Fig. 1 to recreate the VTMD in the laboratory by taking advantage of the unique capabilities of the OMEGA-EP laser.[21,22] For plasma driving, the OMEGA-EP laser features four long-pulse (LP) UV beamlines that can deliver ~ 5 kJ to a 0.100–5.000 mm-diameter spot on the target in a 1–10 ns pulse. In fact, we use the OMEGA-EP's LP beams for dual purposes: first to drive a magnetized, turbulent plasma from a hollow target cone of the lightweight material, e.g., CH, and then to sustain the conditions necessary for the VTMD to grow.

Our first purpose for the LP beams is met at early times t_1 when they turn on to strike the interior surface of the target cone. Plasma is ablated from the laser spots and is initially magnetized by the Biermann battery mechanism.[23,24] The ablated, magnetized plasmas converge towards the axis of the cone where they collide to form a turbulent, magnetized jet directed through the cone opening.

Our second purpose for the LP beams is met at later times t_2 after the turbulent, magnetized plasma jet has pulled into itself enough

material to intercept a significant amount of the LP beam energy before the latter can reach the remnants of the target cone. A hot spot forms in the jet where the laser energy deposition is most intense. In our scheme where multiple LP beams are used as heaters, the hot spot forms where the LP beams intersect each other and the jet.

At the hot spot, the plasma temperature can be sustained by the laser energy deposition over the remaining duration of the pulse such that the resistivity, $\eta \propto T_e^{-3/2}$, of the collisional ($\omega_{p,e}/\omega_{c,e} \sim 100$) plasma is maintained at a lower level than the viscosity, $\nu \propto T_i^{-5/2}$, thereby defining the VTMD criterion. In terms of the dimensionless Reynolds numbers Re and Re$_m$, the VTMD criterion can be expressed with the magnetic Prandtl number Pr$_m \geq 1$, for Pr$_m := $ Re$_m$/Re.

The key to achieving this condition is that ions and electrons heat at different speeds. The laser heating first and quickly acts on the plasma electrons through inverse bremsstrahlung. The ions, on the other hand, are heated by the lasers only indirectly and through far slower electron-ion collisions.[25,26]

B. Observing the turbulent dynamo

The direct sign of the VTMD is the exponentially fast increase in magnetic energy in the plasma where it is active. To measure the magnetic energy evolution in our experimental plasma, we leverage the OMEGA-EP's two high-intensity, short-pulse (SP) IR beamlines to drive target-normal sheath acceleration (TNSA) of a deflectometry imaging proton beam from a hydrogenated planar backlighter.[27,28]

When the beamed protons pass through the turbulent, magnetized plasma jet wherein the VTMD can exist, their trajectories are imprinted with the configuration and strength of the intervening magnetic field. From the deflectometry image formed by all imprinted protons on the far side of the intervening magnetized plasma, we can infer the magnetic energy content and distribution contained in the latter.[29,30]
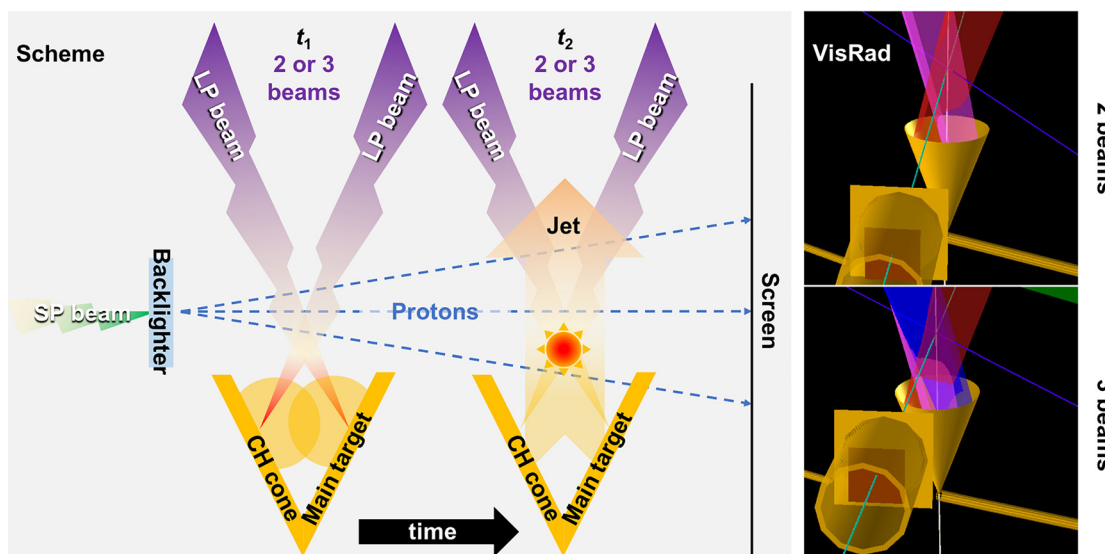
FIG. 1. Left of "screen": the scheme involves the LP beams for a dual purpose—first (t_1) to produce a magnetized jet from ablated cone plasma and then (t_2) to directly heat the jet producing a viscous dissipation-dominated hot spot. The TMD activity is assessed from SP beam-accelerated proton deflectometry imaging of the magnetic fields. Right of "screen": VisRad drawings show the beams and targets in realizable configurations on the OMEGA-EP with a shielded proton backlighter in the foreground.

Because the flight time of the TNSA protons is much shorter than the plasma physics timescales, the deflectometry image they form is a snapshot from the time they are driven. To observe the amplification of magnetic energy by the VTMD, the firing time of the proton-accelerating SP beams can be varied in delay against the plasma-driving LP beams to capture the magnetic energy at different phases of the plasma evolution.

III. NUMERICAL SIMULATIONS

A. Initial conditions

We validate our experimental platform by performing 3-D numerical simulations of our designs using the Eulerian MHD code FLASH.[31] The initial conditions in FLASH are set up to match one-to-one with realizable OMEGA-EP experimental configurations following our scheme.

We begin setting up our initial conditions by building the domain around the main target—a 0.300 mm-thick hollow cone of 1 g/cc CH with an interior space of 2 mm-diameter and 2.74 mm-height filled with a pseudovacuum of 10^{-5} g/cc He $\sim$500 Torr. The vacuum region extends from the cone's opening opposite its apex a farther 4.5 mm. The cone is backed on its exterior to a 8.94 g/cc Cu block sized and hollowed out to flush with its opening, thereby filling out the remainder of the $(2.5\,\text{mm})^2 \times 7.5\,\text{mm}$ domain. The equations of state (EOS) and opacity of both the CH cone and He pseudovacuum are obtained from the atomic database IONMIX,[32] while those of the Cu block are obtained from the atomic database PrOpacEOS.[33]

We introduce into our FLASH domain two or three 0.5 TW UV laser beams in simultaneous 10 ns-duration square pulses using native laser energy deposition methods. The pointings of the simulated laser beams with respect to the target cone follow actual OMEGA-EP constraints as modeled in the HED experimental design tool VisRad.[34] Effectively, we nest our simulation domain in a simulated evacuated OMEGA-EP target chamber. Each wall of the domain is opened to the surrounding vacuum to allow free escape of matter and energy.

For the two-beam configuration, we model EP beams #3 and #4 from ports #63 and #38 with spots shaped using SG8-750 and SG10-400 dispersive phase plates (DPPs). These beams intersect the cone axis at the target chamber center (TCC) $\sim$0.800 mm outside the cone's opening. The simulated cone axis is fixed towards $+90°$ declination to accommodate the proton deflectometry imaging beamline that also goes through the TCC in an orthogonal direction.

For the three-beam configuration, we model EP beams #2, #3, and #4 from ports #64, #63, and #38 with spots shaped using the SG8-750 DPP. These beams intersect the cone axis at the TCC $\sim$0.600 mm outside the cone opening. To accommodate the additional LP beam, the cone is rotated around the TCC by no more than $10°$ from $+90°$ declination.

In addition to native FLASH methods, our simulation required the use of a Biermann battery module courtesy of Prof. P. Tzeferacos of the University of Chicago FLASH Center. We implemented the Biermann battery as a modification to the electric field flux $\vec{E}$, thereby minimizing its contribution to the numerical $\nabla \cdot \vec{B}$.

B. Early times—t_1

We show the early time ($t_1 \in [0, 5]$ ns) formation of the turbulent, magnetized plasma jet from converging laser ablation bubbles in the simulated three beam-driven experiment in Fig. 2. In this sequence, we plot the distribution of the plasma density, with the overlaid magnetic field in a representative slice of the 3-D domain across a diametric plane of the cone.

As time advances through 1.4 ns (from left to right), laser ablation bubbles that are initially magnetized by the Biermann battery are emitted from the interior surface of the cone towards its axis ($x = 0$). They collide, and the resulting plasma is a turbulent, magnetized jet
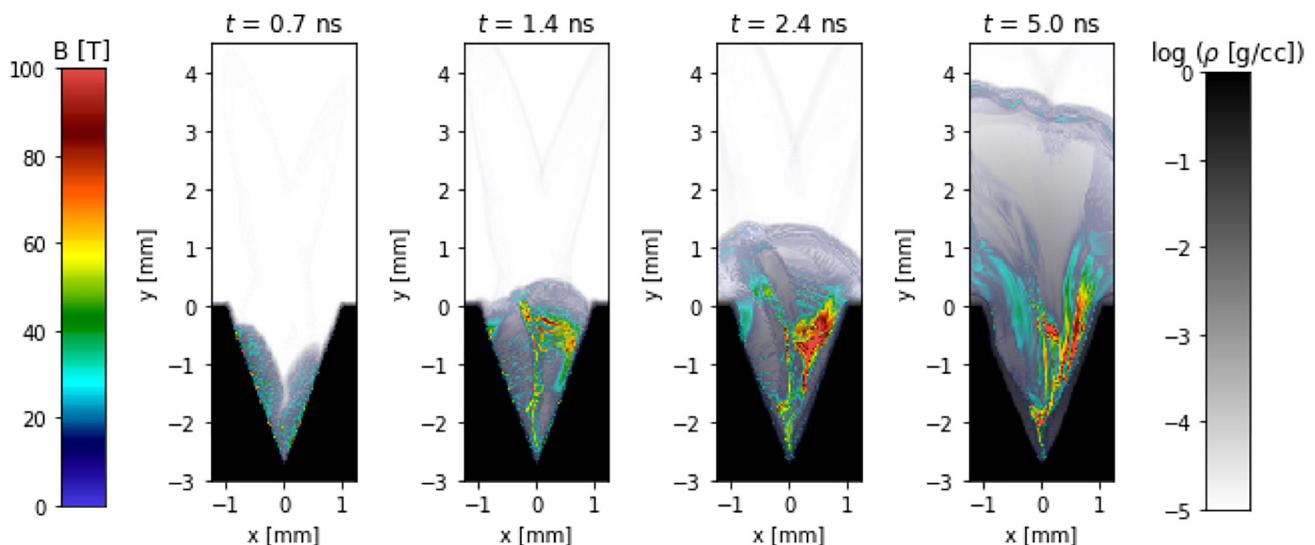
FIG. 2. Early-time ($t_1 \leq 5$ ns) coronal slices map the plasma density and magnetic field in a simulated three-beam experiment in which a turbulent, magnetized jet develops from laser ablation bubbles that converge on the axis ($x = 0$) of the target cone. The ablation bubbles are weakly magnetized by the Biermann battery mechanism at onset, but the magnetic field rapidly strengthens when the bubbles collide.

wherein the magnetic field has become amplified—primarily by compression within the cone ($y < 0$). By 5 ns, the fully developed jet has overtaken the TCC ($x = 0$, $y = 0.600$ mm) through which the LP beams are aimed and where the hot spot for VTMD activity should form.

C. Later times—t_2

We map in Fig. 3 the VTMD conditional variable $\mathrm{Pr_m}$ ($x < 0$), T_e ($x > 0$), and the laser deposition profile at later times in the plasma evolution ($t_2 \in [5, 10)$ ns) at the onset of the hot spot and towards the end of the laser pulse. We plot these quantities in a representative (half-) slice of the 3-D domain across a diametric plane of the cone.

For either two- or three-beam configurations, the hot spot is sustained over the 5 ns remainder of the laser pulse with a nearly one-to-one correspondence between the highest $T_e \gtrsim 1.0$ keV, $\mathrm{Pr_m} \gtrsim 1$, and the most intense region of laser deposition where the LP beams intersect one another and the jet axis ($x = 0$, $y = y_{\mathrm{TCC}}$). That there is little change in the hot spot appearance between onset and laser cutoff times owes to the large-scale steadiness of the underlying plasma outflow from the cone. Where the difference occurs between the two- and three-beam configurations is the size and shape of the hot spot itself.

For the two-beam configuration, one beam has a tighter spot at the TCC of ≈ 0.400 mm-diameter achieved with the SG10-400 DPP, and the other beam has a spot ≈ 0.750 mm achieved with the SG8-750 DPP. The hot spot, i.e., where the VTMD criterion is met with $\mathrm{Pr_m} \gtrsim 1$, is achieved only at the intersection of the much more intense tight beam with the wide beam. For the three-beam configuration, despite all three beams being wide, the extra available power from the

third beam allows the VTMD criterion to be met in a much larger volume. This contrast is reflected in the temperature profile of the hot spot. For the two-beam configuration, T_e can be sustained up to ~1 keV across a tight region. For the three-beam configuration, T_e can be sustained up to ~1.5 keV across a much wider region.

$\mathrm{Pr_m} \propto \nu/\eta$ as shown in Fig. 3 is in fact a partly derived quantity: the resistivity factor η is self-consistently obtained from the MHD simulation physics, while the viscosity factor ν is computed from more primitive quantities only during post-processing.

Real physical viscosity is computationally expensive to simulate. Hence, viscosity in FLASH is implemented using an artificial term that can be tuned to balance accuracy and cost. Although HED experiment simulations using artificial viscosity tend to underestimate diffusion across shocks, e.g., in inertial confinement fusion schemes,[35] our experiment involves rather more inviscid flows at scales we can still accurately model at reasonable cost.

IV. DISCUSSION

A. Environment of the turbulent dynamo

The $\mathrm{Pr_m} \gtrsim 1$ criterion is crucial for the VTMD activity. However, the VTMD also requires seed magnetic fields and turbulence energy. We show in Fig. 4 the contour maps of the vorticity ω—identifying the turbulence eddies—constrained to the hot spot regions. The hot spot-constrained vorticity contours are overlaid on a map of the magnetic field. Where all three ingredients—$\mathrm{Pr_m} \geq 1$, turbulence (kinetic) energy, and magnetic field seeds—for the VTMD overlap, we identify likely regions where the VTMD is active.
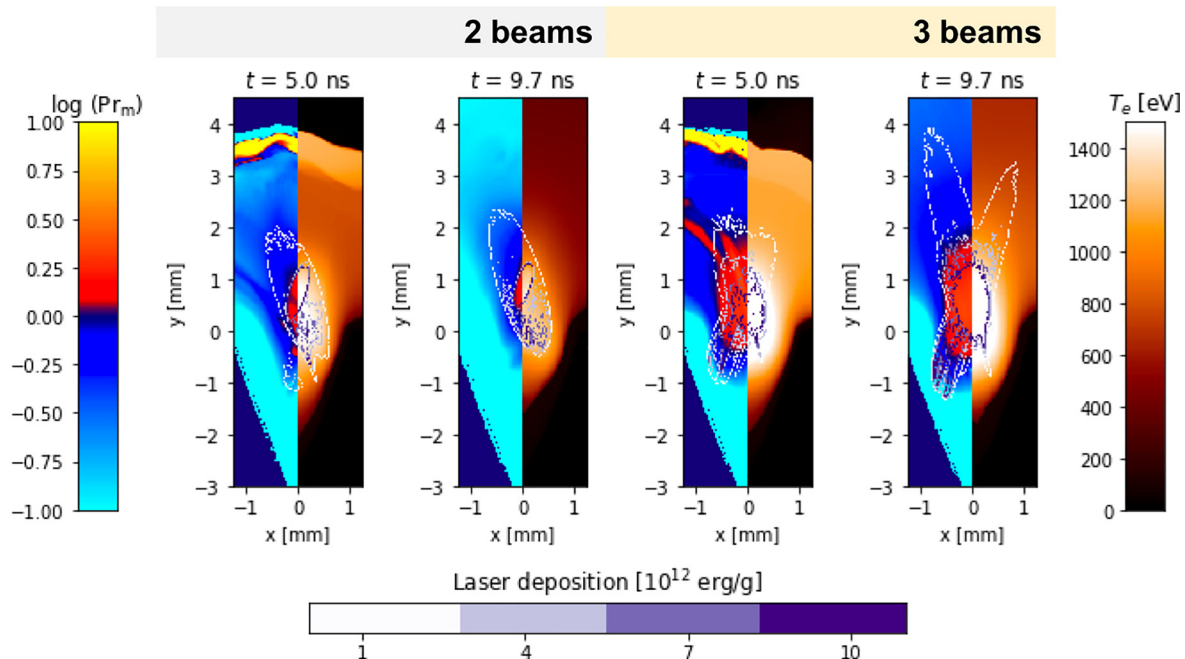
FIG. 3. Later-time ($t_2 > 5$ ns) coronal slices map the strongly correlated plasma magnetic Prandtl number ($x < 0$ halves), electron temperature ($x > 0$ halves), and laser energy deposition profiles for both two- and three-beam configurations both at the onset ($t_2 \to 5$ ns) of the hot spot and through 0.3 ns before the end of the laser pulse ($t_2 \to 9.7$ ns).
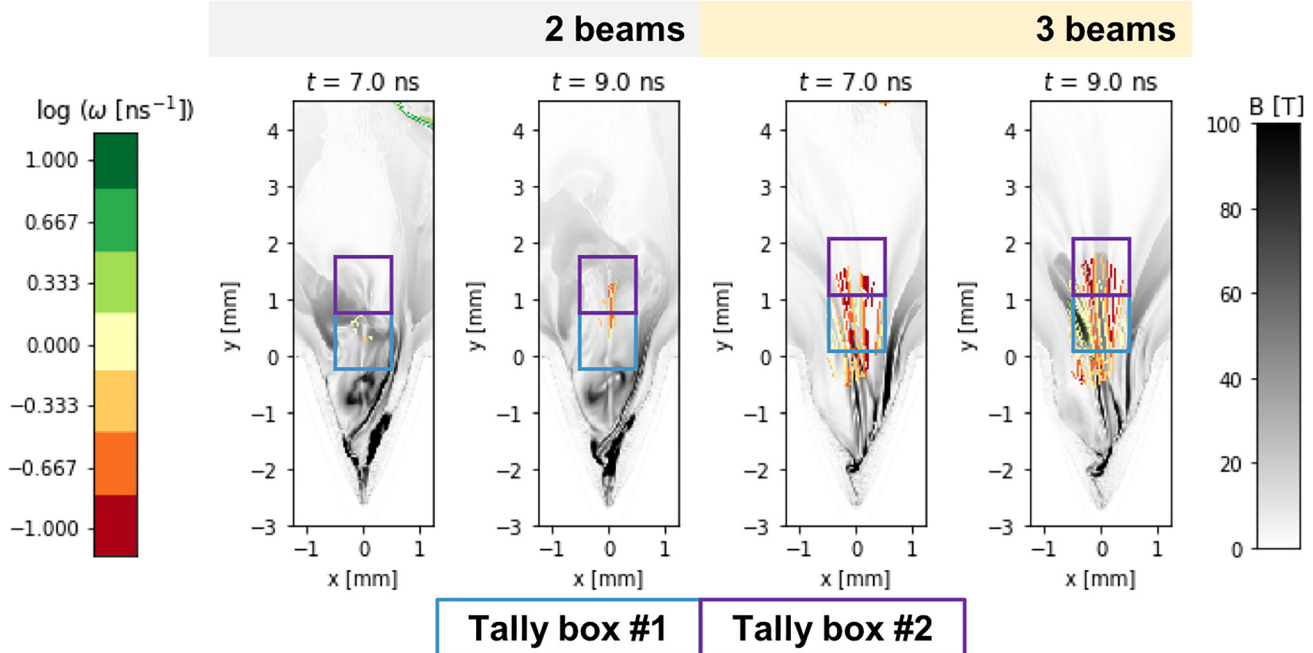
FIG. 4. Later-time ($t_2 > 7$ ns) coronal slices map the hot spot-constrained ($Pr_m \geq 1$) vorticity ω profiles and the magnetic field. The regions where the strong hot spot-constrained vorticity overlaps strong magnetic fields are suggestive of the ongoing VTMD activity. The VTMD energy trajectories of Fig. 5 we discuss in Sec. IV B are obtained by sampling the 1 mm^3 tally boxes overlying the hot spot.

For the two-beam configuration, the hot spot is insubstantial. The regions where the VTMD can exist are likewise confined. Sampling the vorticity and magnetic field over the hot spot returns a single, barely-coherent structure with $\omega \lesssim 0.5$ ns^{-1} that only arises by 9 ns. With $\omega \lesssim 0.5$ ns^{-1} in this region, the dynamo timescale is ~ 2 ns. This implies that the lasers cut off only halfway into a turn of the turbulence eddy, thereby prematurely shutting down any weak, ongoing VTMD activity.

For the three-beam configuration, the much larger hot spot allows a much wider sampling of the colocated turbulence and magnetic field structures where the VTMD can be active. At 7 ns, there already exist in the hot spot significant magnetic field and correlated turbulence eddies with turnover times $\lesssim 1$ ns. By 9 ns, the turbulence and magnetic field mutually reinforce by the VTMD mechanism, producing turbulence eddies with $\omega \sim 3$ ns^{-1} and magnetic filaments with strength approaching 100 T.

B. Trajectory of the turbulent dynamo

We look in Fig. 5 for the sign of the VTMD in the trajectories of the thermal (E_{th}), turbulence kinetic (E_K), and magnetic (E_B) energies. These trajectories show the sum of each type of energy tallied over time from 1 mm^3 boxes we marked over the hot spot in Fig. 4. The hot spot is sampled with two adjacent tally boxes #1 and #2 that are aligned to the flow direction ($+y$) of the jet. Hence, the contrast between the #1 and #2 trajectories shows how the energies evolve in the flow first entering the hot spot (#1) and then having gone through the VTMD (#2).

The two- and three-beam trajectories share some common ground. For example, the passage through the tally boxes of the contact discontinuity (CD) between the jet plasma and the pseudovacuum occurs ~ 2 and ~ 3 ns for #1 and #2 boxes. The bump in magnetic and turbulence kinetic energies immediately following the passage of the CD occurs due to the compression of the supersonic jet plasma against the pseudovacuum into a pseudoshock. Both pseudovacuum and pseudoshock are only artefacts of the Eulerian scheme. For thermal energy, the pseudoshock appears in the pseudovacuum upstream of the CD rather than behind. Following the passage of the pseudoshock, the trajectories begin to diverge in behavior between beam configurations and energy types.

For the two-beam configuration, the jet appears unsteady at the scale of the 1 mm^3 tally boxes. The energy trajectories all fluctuate at a level, and the fluctuations for each tally box are conformal across energy types. These fluctuations have a period of ~ 3 ns and amplitudes of up to a factor of a few for turbulence kinetic and magnetic energies, thereby drowning out the true signal of the VTMD. In fact, the wild fluctuations in the flow are a consequence of the asymmetry of the LP beam spots formed by using different DPPs.

For a two-beam configuration, one tight beam is required to produce a $Pr_m \gtrsim 1$ region of any size. With mirrored beams, however, the turbulence (kinetic) energy seeded into the plasma on jet formation is reduced due to the stronger symmetry of the flow. Furthermore, using two tight beams does not correct the deficit of total energy deposited into the jet—that is the unpardonable sin of two-beam configurations—the hot spot where $Pr_m \gtrsim 1$ must either be confined to a very small region, making it less effective in sustaining the VTMD or it fails to appear altogether.
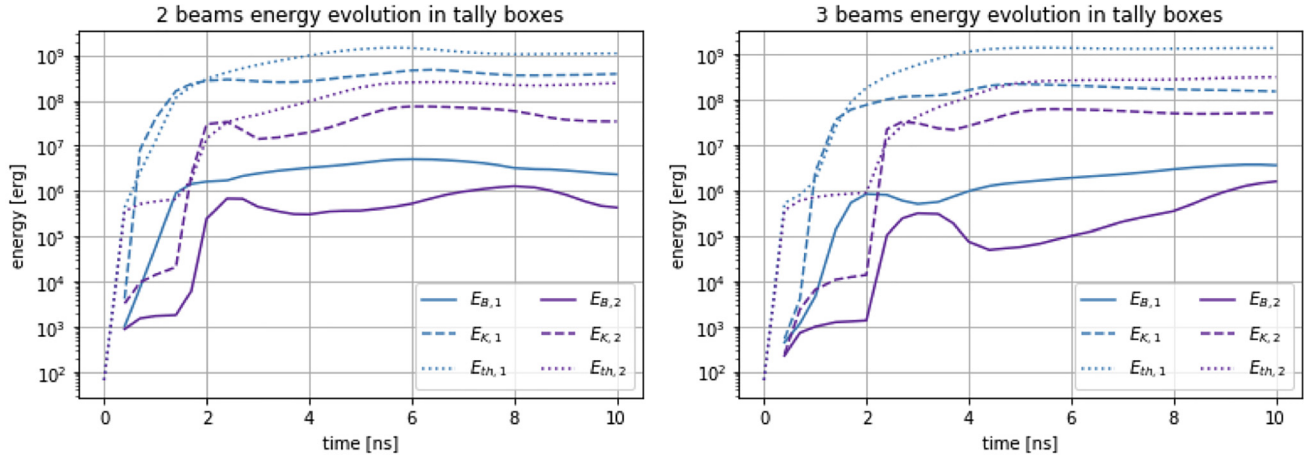
FIG. 5. The thermal, turbulence kinetic, and magnetic energy trajectories are compared between simulations on two-beam and three-beam experimental configurations. For each beam configuration, energy trajectories from each tally box identified in Fig. 4 are distinguished to show the evolution of the VTMD across the hot spot. For the 3-beam configuration, the sign of the VTMD is strongly apparent in the exponential, nearly twenty-fold amplification of the magnetic energy in tally box #2 during $t_2 \in [5, 10)$ ns.

For the three-beam configuration, the jet becomes steady with fluxes of turbulence kinetic and thermal energy flattening out after the passage of the pseudoshock. In this steady jet, the VTMD emerges in the magnetic energy trajectory. Starting just before 5 ns with the onset of the hot spot, the magnetic energy in #1 and #2 begins to climb at nearly constant exponential speed. By the laser cutoff time at 10 ns, the final magnetic energies in boxes #1 and #2 have been amplified from their onset values by factors of 3 and 30 ($\sim$3000% increase) by VTMD and by amounts that are negligible ($\sim$1%) in contrast by both Poynting fluxes and the Biermann battery.

C. Activation of the turbulent dynamo

Where the VTMD is active, it is preceded by an activation condition, the critical $\mathrm{Re}_{m,c}$ that depends on the hardness of the turbulence kinetic energy spectrum. We show in Fig. 6 the evolution over the 10 ns-duration of the UV laser pulse and the turbulence kinetic and magnetic energy spectra $E_{K,B}(k)$ for our three-beam configuration with which we were able to activate (and sustain) the VTMD.

By the onset of identifiable VTMD activity at 5 ns, the turbulence kinetic energy spectra have already settled to a steady state with spectral index $\gamma \lesssim -2$ over $k \in [10\,256]$ cm^{-1}, for $E(k) \propto k^{\gamma}$. The appearance of energy in regions $k < 10$ cm^{-1} and $k > 256$ cm^{-1} is only an artefact of binning the Cartesian 3-D spectra into spherical shells. That the Burgers-like spectra span k_{resolved} from end to end is indicative of the origin of the turbulence in supersonic driving at a high Mach number $\mathcal{M}$ on scales larger than the tally boxes, i.e., the driving scale is imprinted from the target cone geometry with $L \gtrsim 2$ mm ($k \lesssim 5$ cm^{-1}).

In this hard and supersonic turbulence, analytic estimates of $\mathrm{Re}_{m,c}$ are imprecise and predict a range from a few tens to tens of 10^3 s.[14,16,36]
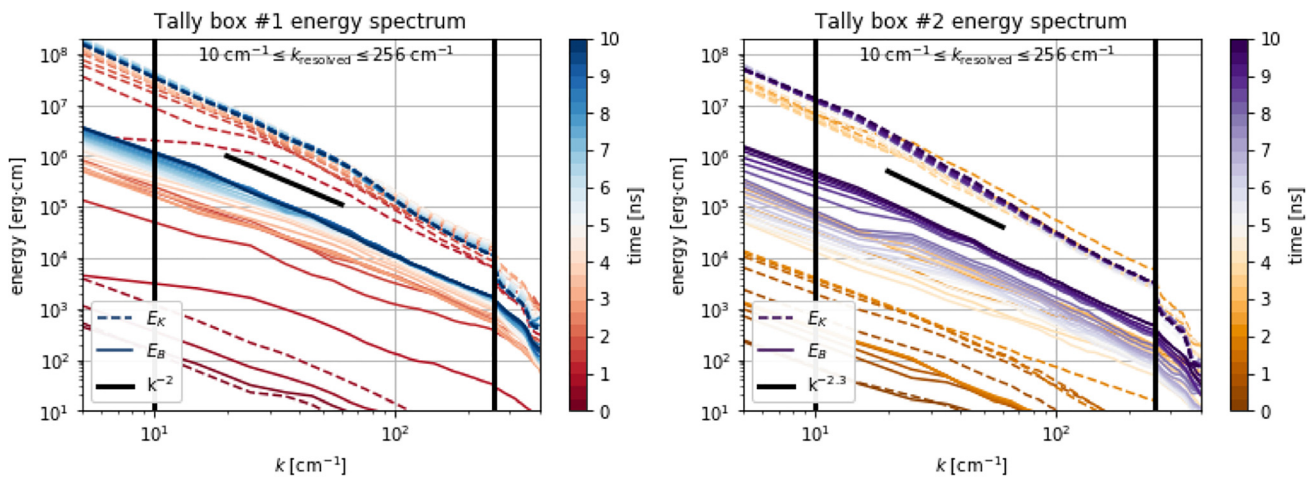
FIG. 6. The turbulence kinetic and magnetic energy spectra for resolved $10 \leq k \leq 256$ cm^{-1} are plotted sequentially for each tally box. The turbulence kinetic energy spectra converge by the onset of quasi-steady flow near 5 ns just as seen in Fig. 5. The magnetic energy freezes for $k > 40$ cm^{-1} by $\times$5 ns for tally box #1 and for $k > 25$ cm^{-1} by $\times$8 ns for tally box #2 when the VTMD saturates on smaller scales. The minimum k where the VTMD is saturated continues to visibly advance towards lower k through the remaining time.

3-D MHD models of the ISM turbulence with similar γ and Pr_m give $Re_{m,c} \gtrsim 100$. This is well within the analytic range, but the latter is so wide that the agreement is trivial.[15]

Obviously, the analytic estimates are not particularly predictive—they likely fail to represent sensitivities to the initial conditions that are only defined in full numerical simulations of specific scenarios. For the same reason, it is difficult to compare between numerical simulations of different TMD scenarios. In this light, our own numerical simulations are an estimate of $Re_{m,c}$ in the special case of our OMEGA-EP experiment. Where we are able to activate the VTMD in the hot spot, $Re_{m,c} \ll 5500$.

D. Growth of the turbulent dynamo

The growth rate Γ of the TMD, for $E_B \propto e^{\Gamma t}$, also depends on Pr_m and γ. Defining a normalized growth rate $\bar{\Gamma} := (L/V)\Gamma$ for the driving scale L and velocity V of the driving turbulence eddies, we naively obtain for our three-beam VTMD $\bar{\Gamma} \sim 1.8$, given a factor $\sim 30\times$ increase in E_B over 5 ns, with $L \gtrsim 2$ mm and $V \gtrsim 300$ km $\cdot$ s^{-1}. However, the driving scale of the turbulence is larger than that of the hot spot where the VTMD can be active. If we limit the size of eddies to those that fit in the hot spot, then $\bar{\Gamma} \sim 2.1$ with $L \sim 1$ mm and $V \lesssim 150$.

Our growth rates are much faster than those from the earlier HED TMD experiment of Tzeferacos *et al.*[19,20] where $\bar{\Gamma} \lesssim 0.4$, given a factor $\sim 200\times$ increase in E_B over 6 ns, with $Pr_m \sim 0.1$, $\gamma \sim -5/3$, $L \sim 0.300$ mm, and $V \sim 300$ km $\cdot$ s^{-1}. They are also much faster than the highly compressible, supersonic ($\mathcal{M} = 11$) ISM model of Federrath *et al.*,[15] where $\bar{\Gamma} \sim 0.45$ with similar TMD parameters to ours—$Pr_m = 2$, $Re = 1600$ ($Re_m = 3200$), and $\gamma \sim -2$.

These incongruities are also apparent in comparison to analytic estimates, e.g., by Schober *et al.*[16] and Bovino *et al.*[14] Between a Kolmogorov turbulence of $\gamma = -5/3$ and our own Burgers-like turbulence, these estimates predict a difference factor of $\sim 200\times$ (faster growth for $\gamma = -5/3$) versus $\sim 0.2\times$ we observe. Worryingly, the trend itself appears to be in the wrong direction altogether!

More likely, our significantly accelerated growth rate in contrast to those from other works arises from the fact that if we consider only the turbulence that fits inside the hot spot, then $\mathcal{M} \sim 0.5$—we are in fact working with an incompressible plasma with the $\gamma \sim -2$ spectrum sustained externally. Combining an incompressible plasma with Pr_m over unity, it is not so surprising that our growth rates can be much faster despite unfavorable (hard) driving conditions. As with the estimates of $Re_{m,c}$, we should again consider that the sensitivity of the TMD to specificity of the scenario makes it difficult to compare directly between analytic or numerical estimates of different scenarios.

E. Saturation of the turbulent dynamo

Returning to our discussion on the spectral evolution of the VTMD, we consider its saturation indicated by increasing overlap and stagnation of $E_B(k)$ in time. This occurs in tally box #1 for large $k > 40$ cm^{-1} by $\times 5$ ns and in tally box #2 for large $k > 25$ cm^{-1} by $\times 7.5$ ns. The saturation levels for a given k for each tally are a few % to $\sim 20\%$. This result is significantly higher than the 3% estimated in the closest ISM model of Federrath *et al.*[15] and again more comparable to those reached in more incompressible plasma.

The advance of the minimum k where the VTMD is saturated for each tally has significance. From the onset of small scale (large k) saturation through the remaining lifetime of the VTMD, the magnetic energy is gained only on increasingly larger scales (smaller k) as the VTMD progressively saturates. However, it is on the largest scales where most of the energy is gained at any time. Hence, the effect of large-k saturation is not obvious in the energy trajectories shown in Fig. 5.

That there is energy to be gained on the largest absolute scales at any time in the VTMD's evolution is a consequence of the prepopulation of the magnetic field distribution with such large scale structures at the onset of the VTMD. Unlike TMDs that must grow bottom-up from microscopic scales, e.g., from galactic nuclei as studied by Xu *et al.*,[37] our experimental VTMD is initiated with macroscopic Biermann battery magnetic fields of a similar scale to OMEGA-EP's LP laser beam spots.

F. Coherent control of the turbulent dynamo

Our next exercise in designing our VTMD experiment demonstrates the coherent control of the VTMD by adjusting the laser pulse timing. We show the results of this three-beam exercise in Fig. 7 in the magnetic energy trajectories between three sets of tallies. Two tallies are repeated from Fig. 4, and a third tally is introduced as an initially 1 mm-diameter, 1 mm-height comoving volume centered 0.170 mm above the cone opening (outline shown over the magnetic field at 7 and 9 ns). Each tally trajectory splits at 7 ns to a nominal (full) path where the laser is sustained through 10 ns and a cut path where it prematurely turns off at 7 ns, thereby terminating the VTMD with the removal of the hot spot that sustains its activity.

When the lasers cut off at 7 ns, the energy trajectories immediately fall from the nominal paths for each tally. At 10 ns, the magnetic energy deficit of the cut trajectories exceeds 30% of the nominal value. Here, we find an alternative method to observe the VTMD in action: in Sec. II B, we proposed that we can observe the VTMD from the evolution of magnetic energy in time—we can instead change the lifetime of the VTMD and infer the activity of the latter from the final state of the magnetic energy.

The key to the coherent control of the VTMD leading to observably diverging magnetic energy trajectories involves once again the plasma electrons. In this case, the electrons' high thermal conductivity confines the hot spot to the volume in the immediate path of the laser beams where conductive heat losses can be immediately replaced. However, taking away the heat source by cutting off the laser beams elicits the same rapid response from the electrons—the hot spot immediately dissipates! With the hot spot disappeared, the VTMD becomes unsustainable as both irresistivity and incompressibility of the plasma are no longer supported, and magnetic energy stops being amplified.

G. Synthetic proton deflectometry

Finally, we performed forward modeling of our primary TNSA proton deflectometry diagnostic to produce the hot spot/VTMD-onset time sequences of synthetic images and spectra ($E_{B,IMAGE}$) we show in Fig. 8.

To synthesize the images, we used the FLASH ProtonImaging module to launch at the chosen times a large number of simulated TNSA protons as Lagrangian tracers through the magnetic field within tally box #2 (where the VTMD can best be observed) as defined
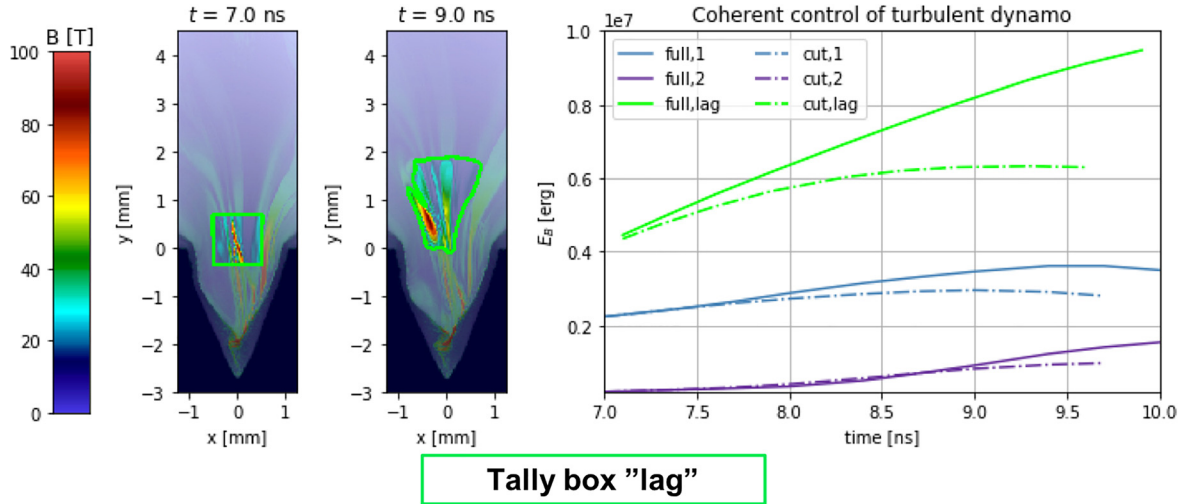
FIG. 7. The magnetic energy trajectories from 7 ns are compared between early (7 ns, "cut") and nominal (10 ns, "full") laser cutoffs for the three-beam configuration. The energy sums—from tally boxes defined in Fig. 4 and from an initially 1 mm-diameter, 1 mm-height cylindrical comoving volume ("lag," green outline)—are plotted over time. On cutoff, the trajectories immediately diverge, and the final energies differ by up to 30% between early and nominal cutoff scenarios.

in Fig. 4. Referring to the scheme of Fig. 1, the simulated protons originate in a point source located 1 cm off the cone axis uprange along the SP beamline from the $(1\,mm)^3$ tally box. The protons form into a $10°$-opening beam that passes through the tally box containing the deflective magnetic fields and ultimately strike a plane detector 27 cm farther downrange.

The detector resolution sets the pixel size equivalent to $10\,\mu m$ at the object plane. The images, then, show the pixel-binned spatial flux distribution of the protons over the detector cropped to the projected size of the $(1\,mm)^3$ tally box and normalized to the average flux density. Crucially, these images are formed using only the

highest effective energy, 40 MeV component of the TNSA proton beam, thereby keeping the deflection of beam protons generally within the small-angle, linear limit most amenable to analysis as demonstrated by Bott et al.[30]

Stepping through the image sequence in time, we find that the flux density indeed remains generally close to the normal value, while unresolvable caustics occupy by far a minority of the space. Furthermore, as time advances, the VTMD activity is observable as the magnetic filaments we previously identified in Fig. 4 gradually strengthen and increase the degree of proton deflection. At the onset of the VTMD $\sim$5 ns, the filaments appear only as weak ripples. By
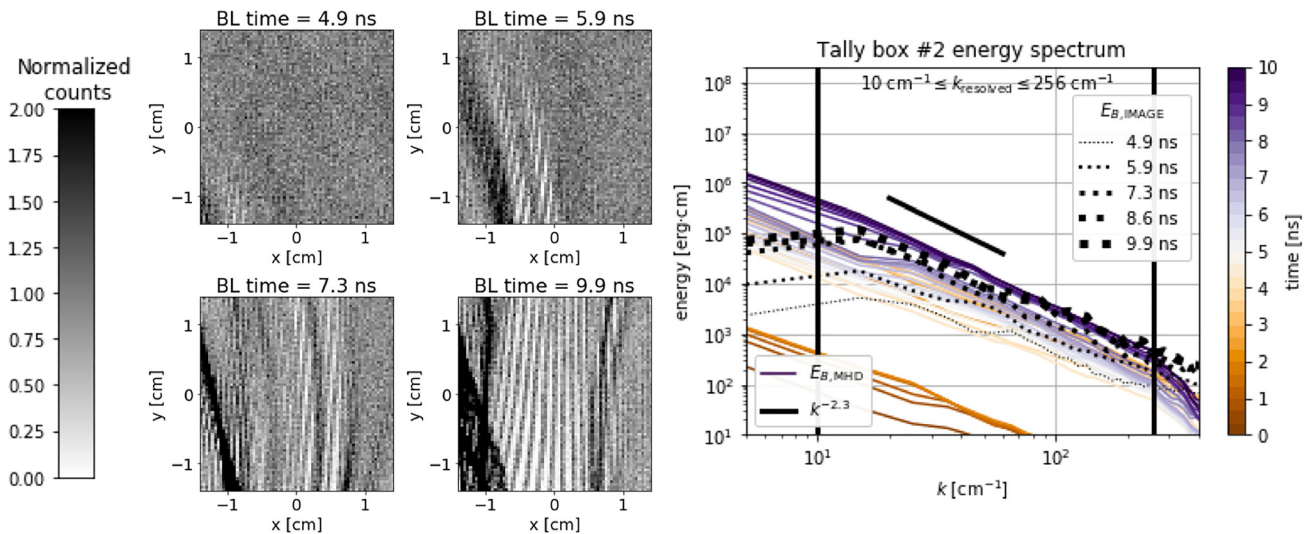
FIG. 8. Time sequence of synthetic proton deflectometry images shows the effects of increasing magnetic energy from the continuous VTMD activity in the sharpening relief of the projected magnetic filaments. The extracted magnetic energy spectra $E_{B,IMAGE}$ quantify the VTMD evolution, in excellent agreement with the physics simulation, $E_{B,MHD}$.

$\gtrsim 7$ ns, the ripples have steepened into sharp relief. However, the images alone help us little to quantify the VTMD, and they should vary immensely from shot-to-shot only from the stochasticity of MHD turbulence.

To properly quantify the VTMD activity using proton deflectometry, we adapt the procedure of Graziani et al.[29] to extract the magnetic energy spectra from the synthetic proton deflectometry images. Overplotting these results in $E_{B,\text{IMAGE}}$ against the sequence of $E_{B,\text{MHD}}$ spectra directly extracted from the MHD simulation shows excellent agreement over k_{resolved}, thereby demonstrating at-a-glance appropriateness of our methods.

Crucially, by extracting the spectra, we reduce the patterns in the images themselves to a form that is agnostic to turbulent stochasticity. As long as the spatial periodicity of image features is comparable, i.e., the TMD environments evolve similarly between shots, the extracted magnetic energy spectra should be robust against shot-to-shot variations between images taken at the same time from initiation. Likewise, a time sequence of spectra from a set of shots should reliably reveal in common a unified trajectory of the VTMD.

V. CONCLUSION

In this article, we introduced a new experimental platform to recreate the VTMD on the OMEGA-EP laser. We showed that as long as the VTMD can exist, then its activity can be observed from its exponential amplification of the magnetic energy by some $30\times$ in the steady flow lasting ~ 5 ns. The normalized growth rate of this VTMD is $\bar{\Gamma} \sim 2.1$, and it progressively saturates from small ($k \gtrsim 30$ cm^{-1}) to larger scales with a few % to ~ 20 % in the time it is observable. Either of these results extrapolates the trends in Pr_m and γ established by recent HED TMD experiments and by numerical ISM models.

Additionally, we conducted analyses to probe the sensitivity of the VTMD activity to the free parameters of our experiment. The most important free parameter affecting the VTMD is the state of the LP laser beams used in a novel role, sustaining a hot spot in the fully developed plasma jet that emerges from the main target cone. In fact, the laser-supported hot spot is the only region in the experimental plasma where the $\text{Pr}_m \gtrsim 1$ criterion can be met to sustain the VTMD activity.

The lasers are able to keep the VTMD criterion where they form the hot spot by their fast, preferential heating of plasma electrons, thereby enhancing the plasma electric conductivity over its viscosity. Conversely, when the laser heating is removed from the plasma, the fast conductive cooling of the plasma electrons dissipates the hot spot just as quickly. The fast and predictive on-off response of the VTMD criterion to the laser state demonstrates coherent control.

Finally, we performed predictive modeling of our primary diagnostic, TNSA proton deflectometry. Our synthetic magnetic energy spectra agreed excellently with those from our physics simulations throughout the evolution of the VTMD, thereby demonstrating that TNSA proton deflectometry imaging combined with the Fourier analysis to extract energy spectra is a robust method to quantify the VTMD activity.

Armed with a more thorough understanding of our experimental platform, we are better positioned to further optimize our design to enhance the visibility of the VTMD or even to extend our scheme to solve real problems in astrophysics.

REFERENCES

[1] A. A. Schekochihin, S. C. Cowley, S. F. Taylor, J. L. Maron, and J. C. McWilliams, Astrophysics **612**, 276 (2004); e-print arXiv:astro-ph/0312046.

[2] R. M. Kulsrud, *Plasma Physics for Astrophysics* (Princeton University Press, 2005).

[3] A. A. Schekochihin, A. B. Iskakov, S. C. Cowley, J. C. McWilliams, M. R. E. Proctor, and T. A. Yousef, New J. Phys. **9**, 300 (2007); e-print arXiv:0704.2002 [physics.flu-dyn].

[4] A. Brandenburg and K. Subramanian, Phys. Rep. **417**, 1 (2005); e-print arXiv:astro-ph/0405052.

[5] T. Inoue, R. Yamazaki, and S-i Inutsuka, Astrophysics **695**, 825 (2009); e-print arXiv:0901.0486 [astro-ph.SR].

[6] P. Padoan, L. Pan, T. Haugbølle, and Å. Nordlund, Astrophysics **822**, 11 (2016); e-print arXiv:1509.04663.

[7] P. Padoan, T. Haugbølle, Å. Nordlund, and S. Frimann, Astrophysics **840**, 48 (2017); e-print arXiv:1702.07270.

[8] C. Federrath and R. S. Klessen, Astrophysics **763**, 51 (2013); e-print arXiv:1211.6433 [astro-ph.sr].

[9] H.-B. Li, A. Goodman, T. K. Sridharan, M. Houde, Z.-Y. Li, G. Novak, and K. S. Tang, *Protostars and Planets VI* (University of Arizona Press, 2014), pp. 101; e-print arXiv:1404.2024.

[10] J. Cho, A. Lazarian, and E. T. Vishniac, Astrophysics **564**, 291 (2002); e-print arXiv:astro-ph/0105235.

[11] J. Cho and A. Lazarian, Mon. Not. R. Astron. Soc. **345**, 325 (2003); e-print arXiv:astro-ph/0301062.

[12] C. Federrath, Mon. Not. R. Astron. Soc. **436**, 1245 (2013); e-print arXiv:1306.3989 [astro-ph.sr].

[13] C. Federrath, G. Chabrier, J. Schober, R. Banerjee, R. S. Klessen, and D. R. G. Schleicher, Phys. Rev. Lett. **107**, 114504 (2011); e-print arXiv:1109.1760 [physics.flu-dyn].

[14] S. Bovino, D. R. G. Schleicher, and J. Schober, New J. Phys. **15**, 013055 (2013); e-print arXiv:1212.3419.

[15] C. Federrath, J. Schober, S. Bovino, and D. R. G. Schleicher, Astrophys. J. Lett. **797**, L19 (2014); e-print: arXiv:1411.4707.

[16] J. Schober, D. R. G. Schleicher, C. Federrath, S. Bovino, and R. S. Klessen, Phys. Rev. E **92**, 023010 (2015); e-print arXiv:1506.02182 [physics.plasm-ph].

[17] R. Monchaux, M. Berhanu, M. Bourgoin, M. Moulin, P. Odier, J.-F. Pinton, R. Volk, S. Fauve, N. Mordant, F. Pétrélis, A. Chiffaudel, F. Daviaud, B. Dubrulle, C. Gasquet, L. Marié, and F. Ravelet, Phys. Rev. Lett. **98**, 044502 (2007).

[18] F. Ravelet, M. Berhanu, R. Monchaux, S. Aumaître, A. Chiffaudel, F. Daviaud, B. Dubrulle, M. Bourgoin, P. Odier, N. Plihon, J.-F. Pinton, R. Volk, S. Fauve, N. Mordant, and F. Pétrélis, Phys. Rev. Lett. **101**, 074502 (2008).

[19] P. Tzeferacos, A. Rigby, A. Bott, A. R. Bell, R. Bingham, A. Casner, F. Cattaneo, E. M. Churazov, J. Emig, N. Flocke, F. Fiuza, C. B. Forest, J. Foster, C. Graziani, J. Katz, M. Koenig, C.-K. Li, J. Meinecke, R. Petrasso, H.-S. Park, B. A. Remington, J. S. Ross, D. Ryu, D. Ryutov, K. Weide, T. G. White, B. Reville, F. Miniati, A. A. Schekochihin, D. H. Froula, G. Gregori, and D. Q. Lamb, Phys. Plasmas **24**, 041404 (2017); e-print arXiv:1702.03015 [physics.plasm-ph].

[20] P. Tzeferacos, A. Rigby, A. Bott, A. Bell, R. Bingham, A. Casner, F. Cattaneo, E. Churazov, J. Emig, F. Fiuza et al., Nat. Commun. **9**, 591 (2018).

[21] L. Waxer, D. Maywar, J. Kelly, T. Kessler, B. Kruschwitz, S. Loucks, R. McCrory, D. Meyerhofer, S. Morse, C. Stoeckl et al., Opt. Photonics News **16**, 30 (2005).

[22] D. Maywar, J. Kelly, L. Waxer, S. Morse, I. Begishev, J. Bromage, C. Dorrer, J. Edwards, L. Folnsbee, M. Guardalben et al., J. Phys.: Conf. Ser. **112**, 032007 (2008).

[23] W. Fu, E. P. Liang, M. Fatenejad, D. Q. Lamb, M. Grosskopf, H.-S. Park, B. Remington, and A. Spitkovsky, High Energy Density Phys. **9**, 336 (2013); e-print arXiv:1209.2150 [astro-ph.HE].

[24] W. Fu, E. P. Liang, P. Tzeferacos, and D. Q. Lamb, High Energy Density Phys. **17**, 42 (2015); e-print arXiv:1409.4273 [astro-ph.HE].

[25]S. I. Braginskii, Rev. Plasma Phys. **1**, 205 (1965).

[26]J. Lindl, Phys. Plasmas **2**, 3933 (1995).

[27]M. Passoni, L. Bertagna, and A. Zani, New J. Phys. **12**, 045012 (2010).

[28]A. B. Zylstra, C. K. Li, H. G. Rinderknecht, F. H. Séguin, R. D. Petrasso, C. Stoeckl, D. D. Meyerhofer, P. Nilson, T. C. Sangster, S. Le Pape, A. Mackinnon, and P. Patel, Rev. Sci. Instrum. **83**, 013511-1–013511-9 (2012).

[29]C. Graziani, P. Tzeferacos, D. Q. Lamb, and C. Li, Rev. Sci. Instrum. **88**, 123507 (2017); e-print arXiv:1603.08617 [physics.plasm-ph].

[30]A. F. A. Bott, C. Graziani, P. Tzeferacos, T. G. White, D. Q. Lamb, G. Gregori, and A. A. Schekochihin, J. Plasma Phys. **83**, 905830614 (2017); e-print arXiv:1708.01738 [physics.plasm-ph].

[31]B. Fryxell, K. Olson, P. Ricker, F. X. Timmes, M. Zingale, D. Q. Lamb, P. MacNeice, R. Rosner, J. W. Truran, and H. Tufo, Astrophys. J. Suppl. **131**, 273 (2000).

[32]J. MacFarlane, Comput. Phys. Commun. **56**, 259 (1989).

[33]J. MacFarlane, I. Golovkin, and P. Woodruff, J. Quant. Spectrosc. Radiat. Transfer **99**, 381 (2006).

[34]J. MacFarlane, J. Quant. Spectrosc. Radiat. Transfer **81**, 287 (2003).

[35]R. Mason, R. Kirkpatrick, and R. Faehl, Phys. Plasmas **21**, 022705 (2014).

[36]J. Léorat, A. Pouquet, and U. Frisch, J. Fluid Mech. **104**, 419 (1981).

[37]H. Xu, H. Li, D. C. Collins, S. Li, and M. L. Norman, Astrophys. J. Lett. **698**, L14 (2009); e-print arXiv:0905.2196 [astro-ph.co].